Remote sensing of the absorption coefficients and chlorophyll *a* concentration in the United States southern Middle Atlantic Bight from SeaWiFS and MODIS-Aqua

Xiaoju Pan,[1] Antonio Mannino,[1] Mary E. Russ,[1,2] and Stanford B. Hooker[1]

Received 7 April 2008; revised 29 August 2008; accepted 19 September 2008; published 29 November 2008.

[1] At present, satellite remote sensing of coastal water quality and constituent concentration is subject to large errors as compared to the capability of satellite sensors in oceanic waters. In this study, field measurements collected on a series of cruises within United States southern Middle Atlantic Bight (SMAB) were applied to improve retrievals of satellite ocean color products from the Sea-viewing Wide Field-of-view Sensor (SeaWiFS) and the Moderate Resolution Imaging Spectrometer (MODIS-Aqua) in order to examine the factors that regulate the bio-optical properties within the continental shelf waters of the SMAB. The first objective was to develop improvements in satellite retrievals of absorption coefficients of phytoplankton (a_{ph}), colored dissolved organic matter (CDOM) (a_g), nonpigmented particles (a_d), nonpigmented particles plus CDOM (a_{dg}), and chlorophyll *a* concentration ([Chl_a]). Several algorithms were compared to derive constituent absorption coefficients from remote sensing reflectance (R_{rs}) ratios. The validation match-ups showed that the mean absolute percent differences were typically <35%, although higher errors were found for a_d retrievals. Seasonal and spatial variability of satellite-derived absorption coefficients and [Chl_a] was apparent and consistent with field data. CDOM is a major contributor to the bio-optical properties of the SMAB, accounting for 35–70% of total light absorption by particles plus CDOM at 443 nm, as compared to 30–45% for phytoplankton and 0–20% for nonpigmented particles. The overestimation of [Chl_a] from the operational satellite algorithms may be attributed to the strong CDOM absorption in this region. River discharge is important in controlling the bio-optical environment but cannot explain all of the regional and seasonal variability of biogeochemical constituents in the SMAB.

Citation: Pan, X., A. Mannino, M. E. Russ, and S. B. Hooker (2008), Remote sensing of the absorption coefficients and chlorophyll *a* concentration in the United States southern Middle Atlantic Bight from SeaWiFS and MODIS-Aqua, *J. Geophys. Res.*, *113*, C11022, doi:10.1029/2008JC004852.

1. Introduction

[2] Satellites such as the Sea-viewing Wide Field-of-view Sensor (SeaWiFS) and the Moderate Resolution Imaging Spectrometer (MODIS) have been widely applied to the study of biogeochemical processes [*International Ocean-Colour Coordinating Group* (*IOCCG*), 1999; *McClain et al.*, 2004]. On the basis of bio-optical theory, the satellite measurement, here remote sensing reflectance (R_{rs}), is often related to inherent optical properties (IOPs) such as the absorption coefficient (a) and scattering coefficient (b) [*Garver and Siegel*, 1997; *Gordon et al.*, 1988; *Kirk*, 1994; *Maritorena et al.*, 2002; *Mobley*, 1994]. IOPs are often related to relevant biogeochemical constituents such as chlorophyll *a* concentration ([Chl_a]), dissolved organic carbon (DOC), particulate organic carbon (POC), and suspended sediment [*Ferrari et al.*, 2003; *Mannino et al.*, 2008; *Rochelle-Newall and Fisher*, 2002; *Siegel et al.*, 2002].

[3] Although chlorophyll *a* pigment plays a critical role in understanding the bio-optical properties in oceanic waters, it is insufficient to fully characterize the biogeochemical properties, especially in coastal waters where colored dissolved organic matter (CDOM) and sedimentary resuspended matter often overwhelm phytoplankton in the contribution to bio-optical properties [*Gordon and Morel*, 1983; *IOCCG*, 2006; *Kirk*, 1994; *Mobley*, 1994]. In general, IOPs are composed of four components: pure water, phytoplankton, CDOM, and nonpigmented particles [*Kirk*, 1994; *Mobley*, 1994]. Absorption from components other than pure water is often considered to be strongly correlated to [Chl_a] in oceanic Case 1 waters, while such an assumption often breaks down in Case 2 waters (e.g., coastal and inland waters) [*Gordon and Morel*, 1983; *IOCCG*, 2000; *Kirk*, 1994; *Mobley*, 1994].

[4] In theory semianalytic (SA) models, which apply spectral deconvolution, are applicable to retrieve constituent

[1]NASA Goddard Space Flight Center, Greenbelt, Maryland, USA.
[2]Goddard Earth Sciences and Technology Center, University of Maryland, Baltimore County, Catonsville, Maryland, USA.

Copyright 2008 by the American Geophysical Union.
0148-0227/08/2008JC004852

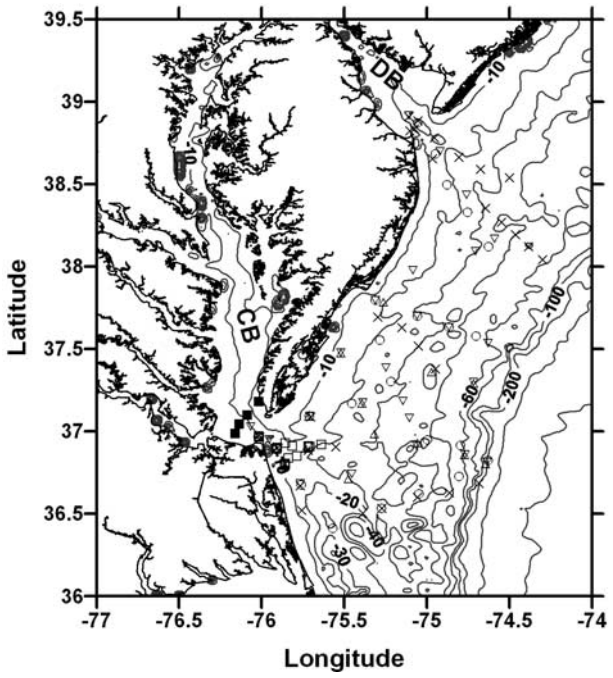

Figure 1. Map of the study area within the southern Middle Atlantic Bight (SMAB). Symbols representing the sampling stations from the following cruises are as follows: BIOME1 (30 March to 1 April 2005) (upward pointing triangles), BIOME2 from 26 to 30 July 2005 (downward pointing triangles), BIOME3 from 5 to 9 May 2006 (circles), BIOME4 from 2 to 6 July 2006 (multiplication signs), Chesapeake Bay Plume with four daily cruises (open squares), and Chesapeake Bay Hydrological survey with ten daily cruises (solid squares).

IOPs from R_{rs} [*IOCCG*, 2006]. For instance, the GSM01 model [*Garver and Siegel*, 1997; *Maritorena et al.*, 2002] produces [Chl_a], absorption coefficient of CDOM and nonpigmented particles (a_{dg}), and particulate backscattering coefficient (b_{bp}). Unfortunately there are at least two problems with SA models applied to coastal waters. First, SA models require detailed knowledge of IOP relationships, which vary regionally or seasonally in coastal waters and in fact are regionally specific or empirically derived [*Babin et al.*, 2003a, 2003b; *Magnuson et al.*, 2004]. Second, SA models are equally sensitive to signals at all wavelengths and require them to be equally accurate. In coastal waters the satellite-derived water-leaving radiances (L_w) at shorter wavelengths (e.g., 412 and 443 nm) often contain some error. Incorrect atmospheric correction due to inadequate information on aerosol absorption and the selection of inappropriate aerosol model, along with the weak signal-to-noise ratio due to strong CDOM absorption, often causes errors on L_w derivation in coastal waters [*Bailey and Werdell*, 2006; *IOCCG*, 2000; *Siegel et al.*, 2000, 2005]. Consequently, the application of SA models in coastal waters faces a significant challenge because of the requirement of highly accurate L_w at all wavelengths.

[5] Empirical algorithms do not require a full understanding of fundamental bio-optical theory. For example, they provide a direct link between satellite-sensed radiance and relevant bio-optical parameters such as [Chl_a] and diffuse attenuation coefficient (K_d) on global and regional scales [*Harding et al.*, 2005; *Mueller*, 2000; *O'Reilly et al.*, 1998, 2000; *Signorini et al.*, 2005]. The creation of empirical algorithms, however, requires a sufficient size of highly accurate field measurements spanning all seasons and adequate spatial coverage for the regions of interest. Thus, empirical algorithms are subject to updates as the data set increases in size. In the work presented here, a set of self-consistent field R_{rs} data is applied to derive absorption coefficients of oceanic constituents in the United States southern Middle Atlantic Bight (SMAB). Absorption coefficients are very important bio-optical properties in the study of radiative transfer modeling and heat budget [*Mobley*, 1994], carbon flux (e.g., [Chl_a], primary production, DOC, and POC) [*Arrigo and Brown*, 1996; *Behrenfeld et al.*, 2005; *IOCCG*, 2006; *Mannino et al.*, 2008; *Marra et al.*, 2007; *Rochelle-Newall and Fisher*, 2002], water quality (e.g., diffuse attenuation coefficient) [*Mueller*, 2000], and oceanic physical processes (e.g., salinity distribution) [*Rochelle-Newall and Fisher*, 2002]. The objectives of this work were (1) to develop and validate satellite algorithms in deriving constituent absorption coefficients for phytoplankton, nonpigmented particles, and CDOM and [Chl_a] near the ocean surface within the SMAB to within ±35% uncertainty; (2) to determine the relative importance of phytoplankton, CDOM, and detritus in sunlight absorption; and (3) to evaluate the seasonal and regional impacts of river discharge on biogeochemical constituents in the SMAB.

2. Methods

2.1. Study Region and Field Experiments

[6] This study focuses on the SMAB from the Delaware Bay (DB) mouth to the region south of the Chesapeake Bay (CB) mouth (Figure 1). This region is well recognized for the significant impacts by riverine discharge from the Delaware and Chesapeake Bays, which account for most of the salinity variability of the SMAB [*Acker et al.*, 2005; *Austin*, 2002; *Harding*, 1994]. The magnitude of freshwater runoff, along with wind and tidal forcing, generates periodic outflow plumes (e.g., winter-spring plume and fall subplume) for this region, and enhances the bio-optical complexity of the SMAB compared to pelagic regions of the Atlantic Ocean [*Acker et al.*, 2005; *Harding*, 1994; *Johnson et al.*, 2001; *O'Reilly and Zetlin*, 1998; *Rennie et al.*, 1999].

[7] Multiple cruises were conducted in this region during 2004–2006, including the Bio-physical Interactions in Ocean Margin Ecosystems cruises (BIOME) during 30 March to 1 April 2005 (BIOME1), 26 to 30 July 2005 (BIOME2), 9 to 12 May 2006 (BIOME3), and 2 to 6 July 2006 (BIOME4), and the Chesapeake Bay Plume cruises (CBP) during 27 May and 3 November 2005, and 6 September and 28 November 2006, and the Chesapeake Bay Hydrological survey (CBH) during 5 May, 5 July, 1 September, 15 October, and 15 November 2004, and 10 January, 26 May, 21 June, 19 August, and 23 September 2005 (Figure 1). The collected bio-optical data included, but not limited to, phytoplankton pigments, IOPs (absorption), and R_{rs} (only on BIOME and CBP cruises in 2005). Water

samples were collected at multiple depths with Niskin bottles.

2.2. Pigments and Absorption Coefficient

[8] Pigment samples were collected on 25 mm GF/F filters under a gentle vacuum (<5 in Hg) and stored in liquid nitrogen in the field before transfer to a −80°C freezer in the laboratory. Pigments were analyzed at Horn Point Laboratory by reverse-phase high-performance liquid chromatography (HPLC) with a C8 column on the HPLC system equipped with photodiode array detector [*Van Heukelem and Thomas*, 2001]. [Chl_a] was calculated as the sum of concentration from monovinyl Chl_a, divinyl Chl_a, and chlorophyllide *a*.

[9] Absorption coefficients of particles (a_p) and nonpigmented particles (a_d) were determined by the quantitative "filter pad" method following the recommendations of *Mitchell et al.* [2002]. Particulate samples were collected on 25 mm GF/F filters under a gentle vacuum (<5 in Hg) and stored in liquid nitrogen in the field before transfer to a −80°C freezer in the laboratory. Nonpigmented particulate samples were defined as the detritus component of particulate samples after two cold methanol extractions (first 5 ml for 10 min, then 10 ml for 1 hour) [*Kishino et al.*, 1985]. Artificial seawater prefiltered through 0.2 μm Whatman Nuclepore filters was used to rinse off methanol and to hydrate the GF/F filters of both blanks and samples. CDOM samples were collected by filtering seawater through precombusted (6 hours at 450°C) GF/F filters and stored under refrigeration (4 to 8°C). In the laboratory, CDOM samples were warmed to room temperature and filtered through 0.2 μm Whatman Nuclepore (polycarbonate) or Gelman Supor (polyethersulfone) filters prior to analysis [*Mannino et al.*, 2008].

[10] Absorbance spectra were measured using a double-beam Cary 100 Bio Ultraviolet-Visible scanning spectrophotometer through 250–800 nm (CDOM in Suprasil quartz 10 cm path length cells) or 300–800 nm (particles) in 1 nm intervals. Blank GF/F filters hydrated with 0.2 μm prefiltered artificial seawater and ultraviolet (UV) oxidized Milli-Q water were used as the blank and reference for particulate absorbance and CDOM absorbance, respectively. Null correction was made by subtracting the mean of absorbance at 790 to 800 nm for particulate samples for each spectrum. No null correction for CDOM absorption was made since the raw absorbance of seawater samples at 690–700 nm was within the noise level of the instrument [*Mannino et al.*, 2008]. The multiple-scattering effect for calculating particulate absorption coefficient (a_p) and nonpigmented particulate absorption coefficient (a_d) was corrected following the method of *Mitchell* [1990], from which nonpigmented particulate samples were assumed to have the same multiple-scattering amplification factor to total particulate samples [*Mitchell et al.*, 2002]. Phytoplankton absorption coefficient (a_{ph}) was calculated as $a_{ph} = a_p - a_d$. The absorption coefficient by CDOM and nonpigmented particles (a_{dg}) was calculated as the sum of a_d and CDOM absorption coefficient (a_g). Total absorption coefficient (a) was calculated as $a = a_w + a_p + a_g$, where pure water absorption coefficient (a_w) was adopted from *Pope and Fry* [1997].

[11] The absorption coefficient from nonpigmented particles, CDOM, or their sum (a_x) was fitted to an exponential function as:

$$a_x(\lambda) = a_x(\lambda_0)\exp[-S_x(\lambda - \lambda_0)] \quad (1)$$

Here, S_x represents the exponential slope for absorption coefficient from nonpigmented particles (S_d), CDOM (S_g), or their sum (S_{dg}). We selected the reference wavelength, λ_0, equal to 380 nm. In equation (1), the wavelengths analyzed were 350 to 600 nm for $a_g(\lambda)$, and 380 to 730 nm for $a_d(\lambda)$ but excluding 400 to 480 nm and 620 to 710 nm to avoid the chlorophyll pigment peaks due to methanol's incapability to extract some pigments as discussed by *Jeffrey et al.* [1997], and 380 to 600 nm (but excluding 400 to 480 nm) for $a_{dg}(\lambda)$ [*Babin et al.*, 2003b].

[12] The phytoplankton absorption coefficient (a_{ph}) is typically related to [Chl_a] as a power function [*Bricaud et al.*, 1995, 1998; *Prieur and Sathyendranath*, 1981]:

$$a_{ph}(\lambda) = A_0(\lambda)[Chl\_a]^{A_1(\lambda)} \quad (2)$$

The modification of equation (2) provides an expression of a_{ph} from its value at a reference wavelength (here 670 nm):

$$a_{ph}(\lambda) = B_0(\lambda)\left[a_{ph}(670)\right]^{B_1(\lambda)} \quad (3)$$

$A_i(\lambda)$ and $B_i(\lambda)$ are derived coefficients. [Chl_a] can also be determined from $a_{ph}(670)$ by a power function similar to equation (3).

2.3. Apparent Optical Properties From in Situ Measurements

[13] The remote sensing reflectance (R_{rs}) spectra (bands centered at 320, 340, 380, 395, 412, 443, 465, 490, 510, 532, 555, 560, 625, 665, 670, 683, 710, 780, and 860 nm, and each band is 10 nm wide at full width half max) were determined with a BioPro in-water profiling spectroradiometer (Biospherical Instruments, Inc., San Diego, CA), as described in detail by *Mannino et al.* [2008]. The instrument was deployed multiple times for each station, and the absolute uncertainty was less than 5%. The R_{rs} at 551 nm was calculated from a linear interpolation of values at 532, 555, and 560 nm [*Mannino et al.*, 2008]. The R_{rs} at 488 nm was assumed to be equivalent to the value at 490 nm. R_{rs} measured at 6 stations during BIOME1 cruise, 19 stations during BIOME2 cruise, and 3 and 6 stations during CBP cruises on 27 May and 3 November 2005 were included for analysis in this paper.

2.4. Satellite Ocean Color Validation

[14] The method to process satellite images was described by *Mannino et al.* [2008] following *Bailey and Werdell* [2006] protocols. SeaWiFS and MODIS-Aqua observations were processed from Level 1 to Level 2 using the SeaWiFS Data Analysis System software (SeaDAS version 5.1.1 and msl12 version 5.6.3). The pixels were masked after atmospheric correction by any of the following flags: land, cloud or ice, high top-of-atmosphere radiance, low normalized water-leaving radiance at 551 or 555 nm, stray light, sun glint, or atmospheric correction failure [*Bailey and Werdell*,

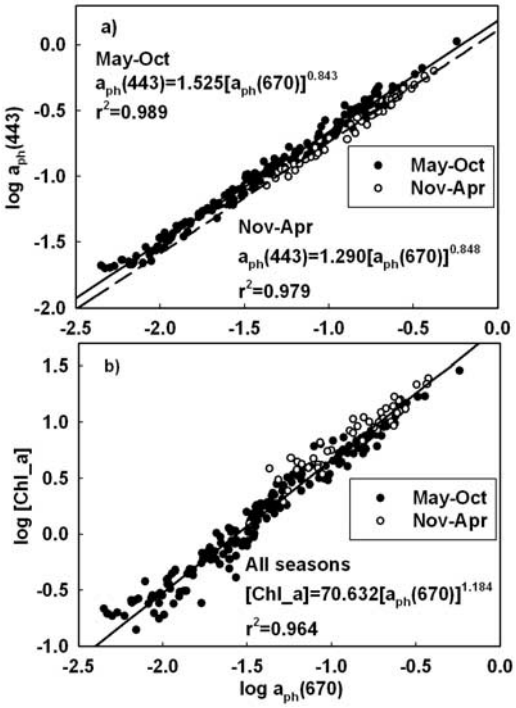

Figure 2. Log-transformed linear regression of phytoplankton absorption coefficient at 670 nm [$a_{ph}(670)$] to (a) $a_{ph}(443)$ and (b) chlorophyll_a concentration [Chl_a]. The solid and dashed lines in Figure 2a represent the regression for summer-fall season (May to October) and winter-spring season (November to April), respectively.

2006]. Pixels with $L_w(412) < 0.2$ mW cm^{-2} μm^{-1} sr^{-1} were excluded to minimize the impacts from atmospheric overcorrection in causing negative or significantly reduced water-leaving radiance [*Siegel et al.*, 2002]. The 3 × 3 pixel arrays centered on the field stations, each with ~1 km resolution (sensor native), were analyzed. The satellite observations which occurred within ±8 hours and ±32 hours of in situ measurements were considered for match-up analysis to allow for inclusion of sufficient data points.

2.5. Analysis and Validation Methods

[15] Three curve-fitting functions, linear function (Model II regression) after log transformation (log_linear_model; equation (4)), fourth-order polynomial function after log transformation similar to OC4V4 [*O'Reilly et al.*, 1998, 2000] (log_polynomial_model; equation (5)), and one-phase exponential decay function (exponential_model; equation (6)), were developed to correlate R_{rs} band ratio to the relevant absorption products:

$$\log[a_i(\lambda)] = C_0(\lambda) + C_1(\lambda)R \tag{4}$$

$$\log[a_i(\lambda)] = D_0(\lambda) + D_1(\lambda)R + D_2(\lambda)R^2 + D_3(\lambda)R^3 + D_4(\lambda)R^4 \tag{5}$$

$$a_i(\lambda) = G_0(\lambda) + G_1(\lambda)\exp\left[-G_2(\lambda)\frac{R_{rs}(\lambda_1)}{R_{rs}(\lambda_2)}\right] \tag{6}$$

Here, $R = \log[R_{rs}(\lambda_1)/R_{rs}(\lambda_2)]$, and λ_1 and λ_2 represent the various bands evaluated, and C_i, D_i and G_i are wavelength-specific derived coefficients, and a_i is the analyzed absorption coefficient as a_{ph}, a_d, a_g, or a_{dg}. In addition, a one-phase exponential function to determine R_{rs} from a_i similar to *Mannino et al.* [2008] was also developed, and a_i was then calculated by its reverse function (reverse_exponential_model; equation (7)):

$$\frac{R_{rs}(\lambda_1)}{R_{rs}(\lambda_2)} = H_0(\lambda) + H_1(\lambda)\exp[-H_2(\lambda)a_i(\lambda)] \tag{7}$$

Four products, $a_{ph}(670)$, $a_d(380)$, $a_g(380)$, and $a_{dg}(380)$, whose surface measurements were represented as the site values, were analyzed with the above equations. The mean absolute percent difference (MAPD) and root mean square error (RMSE) between the modeled products (C_{alg}) and field measurements (C_{field}) were calculated.

$$MAPD = \frac{\sum|(C_{a\lg} - C_{field})/C_{field}|}{N} \times 100\% \tag{8}$$

$$RMSE = \sqrt{\sum (C_{a\lg} - C_{field})^2/N} \tag{9}$$

2.6. Monthly Time Series Analysis

[16] Monthly Level 3 mapped MODIS-Aqua images (4 km resolution) from July 2002 to December 2006 were downloaded from the NASA ocean color website (http://oceancolor.gsfc.nasa.gov) on 8 January 2008. Empirical algorithms developed from this paper were applied to calculate products such as [Chl_a], a_{ph}, a_d, and a_g. Three stations—Location A (75.90°W, 36.93°N), B (75.30°W, 36.93°N), and C (74.77°W, 36.93°N) representing a transect from the Chesapeake Bay mouth to an outer shelf location—were selected and plotted to demonstrate a monthly time series.

3. Results and Discussion

3.1. Absorption Spectra

[17] We observed seasonal transitions in phytoplankton absorption coefficients in April–May and October–November periods. Therefore, at least two seasonal algorithms (May–October and November–April) are required to describe phytoplankton absorption relationships (Figure 2a and Table 1). In general, the phytoplankton absorption ratio [$a_{ph}(\lambda)/a_{ph}(670)$] in May–October is higher than that in November–April (Figure 2a). This coincides with historical observations that the dominant phytoplankton taxa are diatoms in winter and spring, but the phytoplankton assemblage transitions to a greater proportion of dinoflagellates, cryptophytes, and cyanobacteria in summer and fall [*Adolf et al.*, 2006; *Marshall and Alden*, 1993]. Although phytoplankton absorption coefficients are subject to seasonal variation, the relationship between $a_{ph}(670)$ and [Chl_a] (r^2 = 0.964, N = 230) (Figure 2b) is relatively constant

Table 1. Regression Results of Phytoplankton Absorption Coefficient (a_{ph}) to $a_{ph}(670)$[a]

	May–October (N = 196)			November–April (N = 51)		
λ (nm)	B_0	B_1	r^2	B_0	B_1	r^2
412	1.296	0.835	0.986	1.131	0.849	0.987
443	1.525	0.843	0.989	1.290	0.848	0.979
488	1.023	0.846	0.983	0.806	0.821	0.961
490	1.015	0.851	0.983	0.800	0.825	0.963
510	0.842	0.911	0.983	0.637	0.856	0.975
531	0.694	0.983	0.970	0.489	0.875	0.974
551	0.603	1.047	0.945	0.378	0.893	0.956
555	0.587	1.067	0.938	0.347	0.895	0.948
667	0.899	1.005	1.000	0.923	1.012	1.000
678	1.039	1.002	0.999	0.914	0.959	0.994

[a]Results are from equation (3): $a_{ph}(\lambda) = B_0(\lambda)[a_{ph}(670)]^{B_1(\lambda)}$. Log transformation was applied to the data, and Model II linear regression was adopted to calculate $\log[B_0(\lambda)]$ and $B_1(\lambda)$. The selected wavelengths for a_{ph} analysis were the visible bands for SeaWiFS and MODIS-Aqua.

seasonally because of the dominant contribution from Chl_a to $a_{ph}(670)$ [*Jeffrey et al.*, 1997]:

$$[Chl\_a] = 70.632 \times \left[a_{ph}(670)\right]^{1.184} \quad (10)$$

Seasonal variability of riverine discharge, along with other factors such as wind forcing and direction, may cause the seasonal variability of phytoplankton taxonomic composition, pigment package effect, and therefore normalized phytoplankton absorption spectra (Figure 2a) [*Babin et al.*, 2003b; *Bricaud et al.*, 1995, 1998; *Trees et al.*, 2000]. The pigment package effect refers to a consequence of the fact that in the natural waters pigment molecules are not uniformly distributed but are contained within discrete packages such as chloroplasts, cells, and cell colonies, which causes a flattening of the phytoplankton absorption peak because of self shading wherever pigments are localized within cell membranes [*Duyens*, 1956].

[18] Equation (1) described the exponential decay characteristics of a_d, a_g, and a_{dg} rather well with coefficients of determination (r^2) of > 0.95 for a_d, and > 0.99 for a_g and a_{dg}. The exponential slopes (S) covered a wide range with mean ±1 standard deviation of 0.0122 ± 0.0023 (N = 247, ranging from 0.0084 to 0.0260) for a_d, 0.0170 ± 0.0011 (N = 300, ranging from 0.0137 to 0.0221) for a_g, and 0.0148 ± 0.0014 (N = 222, ranging from 0.0122 to 0.0205) for a_{dg}. However, the general exponential decay relationships of S (ordinate) versus absorption coefficients (abscissa) for coastal regions that are significantly impacted by freshwater discharge as suggested by *Carder et al.* [1989] was not apparent for the SMAB data set. Part of the reason was that the data set presented in this paper (Figure 1) did not extend far into the estuaries to cover the full range of water types from freshwater to oceanic waters. The observations above suggest that using mean S values may cause significant errors in predicting a_x spectra. Multiple algorithms to retrieve a_d, a_g, and a_{dg} at multiple wavelengths may be required, as discussed in the next section.

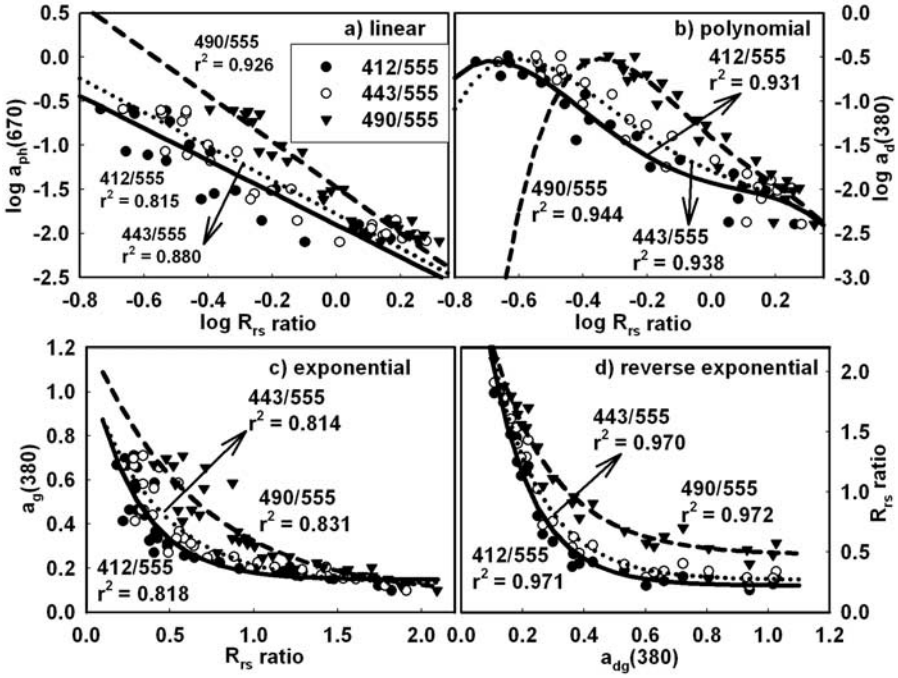

Figure 3. Absorption algorithms derived from field observations of remote sensing reflectance (R_{rs}) from (a) log_linear_model for $a_{ph}(670)$: $\log[a_{ph}(\lambda)] = C_0(\lambda) + C_1(\lambda)R$, where $R = \log[R_{rs}(\lambda_1)/R_{rs}(\lambda_2)]$; (b) log_polynomial_model for nonpigmented particulate absorption coefficient at 380 nm [$a_d(380)$]: $\log[a_d(\lambda)] = D_0(\lambda) + D_1(\lambda)R + D_2(\lambda)R^2 + D_3(\lambda)R^3 + D_4(\lambda)R^4$; (c) exponential_model for CDOM absorption coefficient at 380 nm [$a_g(380)$]: $a_g(\lambda) = G_0(\lambda) + G_1(\lambda)\exp[-G_2(\lambda)\frac{R_{rs}(\lambda_1)}{R_{rs}(\lambda_2)}]$; and (d) reverse_exponential_model for absorption coefficient by nonpigmented particles plus CDOM at 380 nm [$a_{dg}(380)$] $\frac{R_{rs}(\lambda_1)}{R_{rs}(\lambda_2)} = H_0(\lambda) + H_1(\lambda)\exp[-H_2(\lambda)a_{dg}(\lambda)]$. Regression lines from R_{rs} band ratios of 412/555, 443/555, and 490/555 are represented as solid, dotted, and dashed lines, respectively.

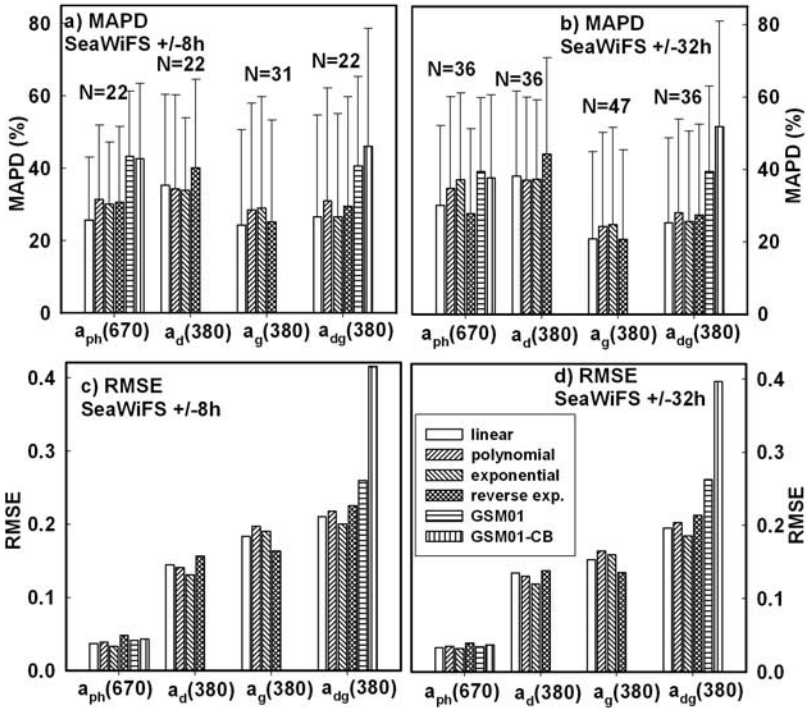

Figure 4. Validation results comparing SeaWiFS observations with field measurements of $a_{ph}(670)$, $a_d(380)$, $a_g(380)$, and $a_{dg}(380)$ from multiple models (log_linear_model, log_polynomial_model, exponential_model, and reverse_exponential_model). (a, b) The mean absolute percent difference. (c, d) The root mean square error. The satellite overpass windows within 8 hours (Figures 4a and 4c) and 32 hours (Figures 4b and 4d). The data from stations applied to develop the algorithms were not included in this analysis. The satellite-derived $a_{ph}(670)$ and $a_{dg}(380)$ from GSM01 model [*Maritorena et al.*, 2002] and GSM01-CB model [*Magnuson et al.*, 2004] are also shown for comparison.

3.2. Algorithm Development and Validation

[19] Three R_{rs} band ratios (412/555, 443/555, and 490/555 for SeaWiFS, and 412/551, 443/551, and 488/551 for MODIS-Aqua) were compared to determine the best algorithm performance. No matter which of the curve-fitting models from equations (4), (5), (6), and (7) was selected, algorithms based on R_{rs} band ratio at 490/555 or 488/551 performed similar to, or better than, the other two band ratios. Figure 3 shows examples of model performance on predicting $a_{ph}(670)$, $a_d(380)$, $a_g(380)$, and $a_{dg}(380)$ from equations (4), (5), (6), and (7), respectively. Performance from other models, i.e., equation (4) on predicting $a_d(380)$, $a_g(380)$, and $a_{dg}(380)$, showed similar results to Figure 3 (data not shown). Because of the possibly poor quality of satellite water-leaving radiance at shorter wavelengths (e.g., 412 and 443 nm) in coastal waters [*Bailey and Werdell*, 2006; *Siegel et al.*, 2002], we selected R_{rs} band ratios at 490/555 or 488/551 for further analysis. Although the selection of only two bands will cause interdependence of satellite-derived products, it still provides valuable information on bio-optical properties of the SMAB in the absence of appropriate semianalytic algorithms based on more bands.

[20] The log_linear_model (equation (4)) proved suitable to validate satellite-derived a_{ph}, a_d, and a_{dg} with relatively high r^2 and relatively low MAPD and RMSE (Figures 4 and 5 and Table 2). The r^2 for the log_linear_model ranged from 0.92 to 0.93 for all three products of $a_{ph}(670)$, $a_d(380)$, and $a_{dg}(380)$, while 0.84 to 0.95 for the other three models. The MAPD for the log_linear_model was typically similar to, or lower than, the other three models, regardless of the satellite sensor (SeaWiFS or MODIS-Aqua) and overpass satellite/in situ time window selected (±8 hours or ±32 hours) (Figures 4a, 4b, 5a, and 5b). This was also supported by the validation results from the RMSE comparisons (Figures 4c, 4d, 5c, and 5d). The exponential_model may provide lower MAPD and RMSE in some cases (Figures 4 and 5), but was not selected because of its relatively low r^2 (0.84 to 0.87). In contrast, the reverse_exponential_model yielded the best validation results for $a_g(380)$ with the highest r^2 (0.90 versus 0.77–0.86) and typically lowest MAPD and RMSE (Figures 4 and 5 and Table 4) as compared to the other models. *Mannino et al.* [2008] showed the same model for a_g but did not include the CBH stations in their validation analysis. The selected R_{rs} band ratio models can also be applied to derive a_d, a_g, and a_{dg} at multiple wavelengths (Tables 2 and 3). Except for the higher MAPD for a_d (34.8–57.5% for SeaWiFS and 41.9–65.3% for MODIS-Aqua), the selected regression methods typically limited MAPD for a_g and a_{dg} to within 30% for wavelengths between 350 and 555 nm (Table 4). The exponential decay slopes (S) for a_d, a_g, and a_{dg} can be derived from nonlinear regression methods with R_{rs} band ratio models at multiple wavelengths (e.g., 355, 380, 400, 412, 443, 490, 510, 531, and 555), and agree reasonably well with field derivations (Table 4). The GSM01 [*Garver and Siegel*, 1997; *Maritorena et al.*, 2002] and its regional version

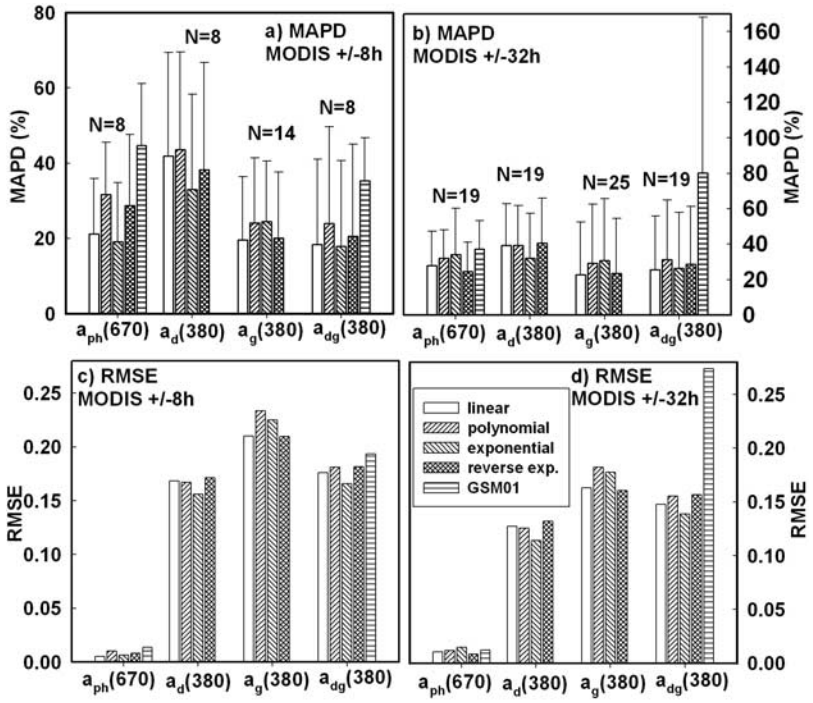

Figure 5. Validation results comparing MODIS-Aqua observations with field measurements of $a_{ph}(670)$, $a_d(380)$, $a_g(380)$, and $a_{dg}(380)$ from multiple models. See Figure 4 for details.

(GSM01-CB) [*Magnuson et al.*, 2004] resulted in relatively high MAPD and RMSE when compared with the field measurements (Figures 4 and 5). The GSM01 model was developed for global ocean application, and thus is not optimized for the variability of in-water constituents observed in nearshore coastal regions, such as variable or region-specific S values. However, even the optimized GSM01 model for this coastal region (GSM01-CB; primarily Chesapeake Bay and nearshore coastal ocean) developed by *Magnuson et al.* [2004] did not perform significantly better than GSM01, e.g., MAPD = 42.6% and 46.0% for $a_{ph}(670)$ and $a_{dg}(380)$ from GSM01-CB, versus 43.3% and 40.7% from GSM01 for SeaWiFS ±8 hour overpass window (Figures 4 and 5). The lack of adequate knowledge of backscattering coefficients, as well as the higher uncertainty of R_{rs} at shorter wavelengths (e.g., 412 and 443 nm) from satellite measurements, may account for the performance of GSM01 and GSM01-CB for this region [*Bailey and Werdell*, 2006; *IOCCG*, 2000; *Magnuson et al.*, 2004; *Siegel et al.*, 2000, 2005].

[21] By applying the regression results shown in Table 1, phytoplankton absorption coefficients at other visible wavelengths can also be derived from $a_{ph}(670)$, which can be derived from satellite radiance observations as shown in Table 2. The validation match-ups based on this approach yielded similar MAPD accuracy levels for $a_{ph}(\lambda)$ at 412, 443, 488, 490, 510, 667, and 678 nm to $a_{ph}(670)$ (21.5–26.1% versus 25.7% for SeaWiFS and 19.0–28.1% versus 21.2%

Table 2. Statistical Results for Absorption Coefficients of Phytoplankton (a_{ph}), Nonpigmented Particles (a_d), and CDOM Plus Nonpigmented Particles (a_{dg}) at Selected Wavelengths[a]

	$R_{rs}(490)/R_{rs}(555)$			$R_{rs}(490)/R_{rs}(551)$		
Parameter	C_1	C_0	r^2	C_1	C_0	r^2
$a_{ph}(670)$	−2.602	−1.467	0.921	−2.769	−1.487	0.923
$a_d(380)$	−2.797	−1.319	0.933	−2.976	−1.340	0.932
$a_d(400)$	−2.812	−1.387	0.933	−2.992	−1.408	0.931
$a_d(412)$	−2.849	−1.427	0.933	−3.031	−1.449	0.931
$a_d(443)$	−3.048	−1.633	0.925	−3.243	−1.656	0.924
$a_d(490)$	−3.260	−1.950	0.902	−3.468	−1.975	0.902
$a_d(510)$	−3.584	−2.105	0.864	−3.813	−2.132	0.864
$a_d(531)$	−3.676	−2.223	0.848	−3.911	−2.251	0.848
$a_d(555)$	−3.315	−2.297	0.891	−3.526	−2.322	0.891
$a_{dg}(380)$	−1.394	−0.434	0.919	−1.487	−0.445	0.919
$a_{dg}(400)$	−1.489	−0.576	0.921	−1.588	−0.587	0.920
$a_{dg}(412)$	−1.535	−0.651	0.922	−1.637	−0.663	0.922
$a_{dg}(443)$	−1.593	−0.879	0.923	−1.698	−0.891	0.923
$a_{dg}(490)$	−1.649	−1.190	0.910	−1.758	−1.203	0.910
$a_{dg}(510)$	−1.725	−1.308	0.899	−1.840	−1.322	0.899
$a_{dg}(531)$	−1.633	−1.406	0.885	−1.743	−1.419	0.886
$a_{dg}(555)$	−1.983	−1.564	0.822	−2.117	−1.580	0.823

[a]Results are from log_linear_model: $\log[a_x(\lambda)] = C_0(\lambda) + C_1(\lambda)R$, where $R = \log[R_{rs}(\lambda_1)/R_{rs}(\lambda_2)]$. The size of the data set is N = 25.

Table 3. Statistical Results for CDOM Absorption Coefficient (a_g) at Selected Wavelengths[a]

	$R_{rs}(490)/R_{rs}(555)$				$R_{rs}(490)/R_{rs}(551)$			
Parameter	H_0	H_1	H_2	r^2	H_0	H_1	H_2	r^2
$a_g(355)$	0.538	3.149	3.978	0.882	0.546	2.805	3.844	0.879
$a_g(380)$	0.534	3.015	6.110	0.902	0.542	2.692	5.909	0.900
$a_g(400)$	0.540	2.940	8.656	0.915	0.547	2.625	8.366	0.912
$a_g(412)$	0.523	2.849	9.914	0.916	0.531	2.551	9.592	0.914
$a_g(443)$	0.531	2.857	17.700	0.908	0.539	2.557	17.130	0.906
$a_g(490)$	0.547	3.138	39.960	0.891	0.555	2.798	38.690	0.890
$a_g(510)$	0.493	2.352	39.870	0.857	0.503	2.126	38.640	0.858
$a_g(531)$	0.494	2.271	50.240	0.829	0.504	2.056	48.700	0.831
$a_g(555)$	0.335	1.798	40.690	0.795	0.346	1.657	39.120	0.799

[a]Results are from the reverse_exponential_model. Model is $\frac{R_{rs}(\lambda_1)}{R_{rs}(\lambda_2)} = H_0(\lambda) + H_1(\lambda)\exp[-H_2(\lambda)a_g(\lambda)]$. The size of the data set is N = 34.

Table 4. Mean Absolute Percent Difference and Root Mean Square Error From Validation Match-Ups for a_{ph}, a_d, a_g, and a_{dg} at Selected Wavelengths[a]

	SeaWiFS (±8 hours)		SeaWiFS (±32 hours)		MODIS (±8 hours)		MODIS (±32 hours)	
Parameter	MAPD	RMSE	MAPD	RMSE	MAPD	RMSE	MAPD	RMSE
$a_{ph}(443)$	23.5	0.0501	23.4	0.0470	23.4	0.0137	23.1	0.0206
$a_{ph}(670)$	25.7	0.0371	30.1	0.0329	21.2	0.0051	27.8	0.0106
[Chl_a]	32.3	3.6808	32.5	3.0339	28.8	3.2805	29.3	2.5474
$a_d(380)$	35.3	0.1447	38.2	0.1350	41.9	0.1684	39.3	0.1275
$a_d(443)$	41.8	0.0787	42.1	0.0726	50.5	0.0876	44.6	0.0664
S_d	13.4	0.0018	11.7	0.0016	11.5	0.0014	12.1	0.0015
$a_g(380)$	25.2	0.1636	20.7	0.1359	20.1	0.2096	23.4	0.1607
$a_g(443)$	22.8	0.0516	20.1	0.0432	20.1	0.0662	21.5	0.0509
S_g	5.8	0.0011	5.5	0.0011	5.2	0.0011	6.7	0.0012
$a_{dg}(380)$	26.5	0.2104	25.2	0.1965	18.4	0.1761	25.6	0.1478
$a_{dg}(443)$	24.4	0.0923	24.4	0.0870	22.1	0.0896	23.1	0.0711
S_{dg}	11.9	0.0020	12.7	0.0021	15.5	0.0024	15.1	0.0023

[a]The derived exponential decay slope (S) for a_d (S_d), a_g (S_g), and a_{dg} (S_{dg}) from nonlinear regression and chlorophyll a concentration ([Chl_a]) are also compared. Data used for algorithm development are not included in this analysis. The size of the data sets are N = 22, 36, 8, and 19 for a_{ph}, a_d, or a_{dg}; N = 29, 45, 14, and 25 for [Chl_a]; and N = 31, 47, 14, and 25 for a_g for SeaWiFS ±8 and ±32 hour and MODIS ±8 and ±32 hour overpass windows, respectively. MAPD, mean absolute percent difference; RMSE, root mean square error.

for MODIS-Aqua), but relatively higher MAPD at 531, 551, and 555 nm (27.2–30.9% for SeaWiFS and 33.1–43.1% for MODIS-Aqua) because of the relatively higher measurement errors from weaker absorption at these wavelengths (Table 4). If we exclude those stations with extremely low a_{ph} (e.g., <0.003 m^{-1} at 555 nm), the MAPD for $a_{ph}(\lambda)$ was at the same accuracy level for all visible wavelengths evaluated. The satellite derivation of [Chl_a] from equation (10) had slightly lower but still reasonable accuracy level compared to that for $a_{ph}(670)$ with MAPD of 32.3 ± 28.2% (N = 29) for SeaWiFS and 28.8 ± 20.6% (N = 14) for MODIS-Aqua (Table 4).

[22] The validation match-ups between field measurements of absorption constituents and satellite derivations within ±8 hours demonstrated reasonable agreement (Figures 6 and 7). The SeaWiFS and MODIS-Aqua match-ups have similar r^2 varying from 0.80 to 0.97, and show slope values from 0.52 to 0.73 and from 0.46 to 0.80, respectively.

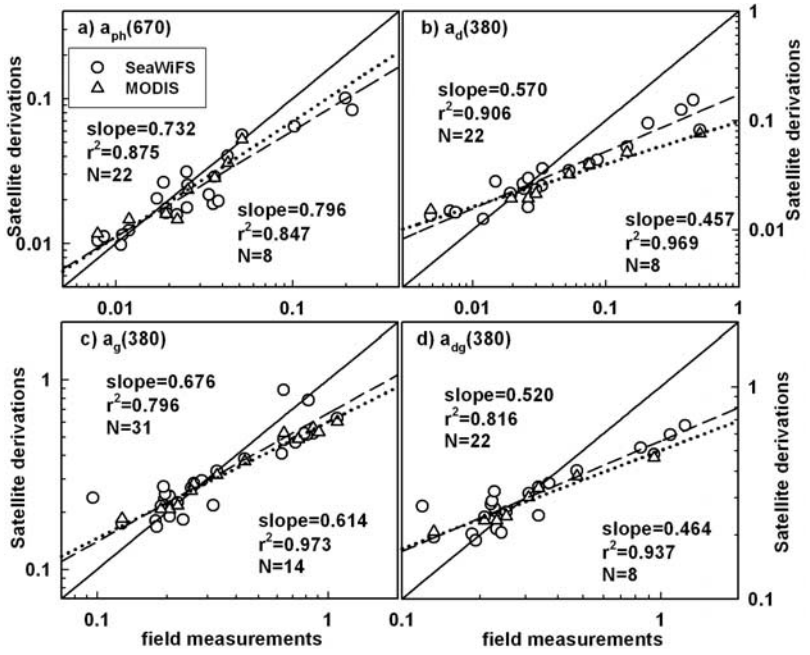

Figure 6. Comparisons of SeaWiFS and MODIS-Aqua and field observations of the absorption coefficients of (a) $a_{ph}(670)$, (b) $a_d(380)$, (c) $a_g(380)$, and (d) $a_{dg}(380)$. The values are plotted on log scale. The satellite derivations of $a_{ph}(670)$, $a_d(380)$, and $a_{dg}(380)$ were from the log_linear_model, while $a_g(380)$ was from the reverse_exponential_model. The match-ups procedure is limited to within ±8 hours, and the data from stations used to develop algorithms are excluded for validation analyses. The statistical results are based on log transformation of the data and shown in Figure 6a for SeaWiFS and Figure 6d for MODIS-Aqua. The solid lines represent the 1:1 lines, while dashed lines and dotted lines represent the regression for SeaWiFS and MODIS-Aqua, respectively.

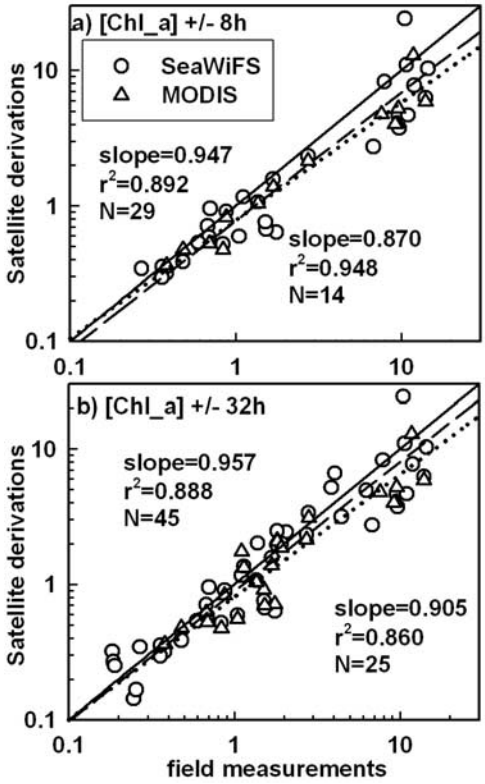

Figure 7. Comparisons of SeaWiFS and MODIS-Aqua and field observations of [Chl_a] for satellite overpass window of (a) ±8 hours and (b) ±32 hours. The data from stations used to develop algorithms of a_{ph} are excluded for this analysis. The solid lines represent the 1:1 lines, while dashed lines and dotted lines represent the regression for SeaWiFS and MODIS-Aqua, respectively. See Figure 6 for detail.

Including the stations applied to develop the algorithms, which increases data set size by 10–12 points for SeaWiFS and 5–6 points for MODIS-Aqua, yielded improvements in all the slopes (e.g., 0.73–0.87 for SeaWiFS and 0.57–0.64 for MODIS-Aqua). When extending the match-up data set from ±8 hours to ±32 hours of the satellite overpass window, similar improvements were also found because of significant increase of data set size by 50% to 140% (data not shown). The validation match-ups between field measurements of [Chl_a] and satellite derivations after log transformation agreed well with r^2 = 0.86 to 0.95, slope = 0.87 to 0.96, and RMSE = 0.20 to 0.24 (Figure 7). Similar statistical results were found for $a_{ph}(670)$ when including those stations used to develop the algorithms (data not shown). It implies that these empirical algorithms are relatively successful and should improve as the size of the data set increases.

[23] Above all, the satellite-derived absorption coefficients from selected functions (log_linear_model for a_{ph}, a_d, and a_{dg}, and reverse_exponential_model for a_g) yielded relatively good results for the SMAB. Since the data set used for algorithm development did not include stations from the CBH cruises (because AOP data was not collected at those stations), the validation analyses should improve after excluding those CBH stations. For example, MAPD improved from 25.7% to 21.9% for $a_{ph}(670)$, from 35.3% to 29.5% for $a_d(380)$, from 25.2% to 20.9% for $a_g(380)$, from 26.5% to 23.8% for $a_{dg}(380)$, and from 32.3% to 24.2% for [Chl_a] for SeaWiFS ±8 hour overpass time window. Therefore, in the future the addition of complete data sets from the lower bay locations will expand the dynamic range of the algorithms and may significantly improve the model capability in more turbid areas of the SMAB.

3.3. Seasonal Variability

[24] These empirical algorithms can be applied to study the spatial and seasonal variability of coastal ocean constituents. Figure 8 shows typical examples of the spatial distribution of the absorption coefficients within the SMAB during four seasons: summer (June–August), fall (September–November), winter (December–February), and spring (March–May). The satellite images clearly show the gradients from high to low constituent concentration between the coast and the open ocean as well as the riverine/estuarine outflow impact along the coast (Figure 8). The seasonal variability of phytoplankton absorption [e.g., $a_{ph}(443)$] may be due primarily to the river discharge rate from the bay mouths [*Acker et al.*, 2005; *Adolf et al.*, 2006; *Marshall and Alden*, 1993; *Marshall et al.*, 2006]. The monthly mean flow rates out of the Chesapeake Bay for these selected images were 510, 1648, 2983, and 1463 $m^3 s^{-1}$ for August 2005, November 2005, February 2006, and May 2006, respectively (data are available at http://waterdata.usgs.gov/nwis/) (G. Fisher, U.S. Geological Survey, personal communication, 2007). Consequently, lower phytoplankton abundance occurred during the dry season in summer 2005 compared to the other three seasons. The seasonal variability of detritus absorption [e.g., $a_d(443)$] is complex. At least two primary sources of detritus from riverine/estuarine outflow and sedimentary resuspension controlled a_d in the SMAB. The significant contribution from storm-driven sedimentary resuspension in autumn may explain the higher detritus content in November 2005. The seasonal variability of CDOM absorption [e.g., $a_g(443)$] may be controlled primarily by the degree of riverine inputs of degraded terrestrial vegetation to the SMAB [*Del Vecchio and Blough*, 2004; *Mannino et al.*, 2008].

[25] CDOM plays a critical role in contributing to sunlight absorption and thus impacts primary production in the SMAB by reducing the amount of photosynthetically active radiation (PAR) available for phytoplankton growth [*Arrigo and Brown*, 1996]. At 443 nm, CDOM accounted for 35–70% of total light absorption excluding water absorption (a_{pg}), as compared to 0–20% for nonpigmented particles, and 30–45% for phytoplankton (Figures 9 and 10). Pure seawater absorption ($a_w(443) \approx 0.007\ m^{-1}$) [*Pope and Fry*, 1997] typically accounts for a negligible fraction (~3.0%) of $a(443)$ in the SMAB. The relatively low contribution of detritus absorption within coastal ocean regions was also reported by *Siegel et al.* [2002] and may explain the performance of the satellite-derived $a_d(\lambda)$ in the validation analysis (Table 4 and Figures 4, 5, and 6). The satellite-derived $a_d(\lambda)$ underestimates $a_d(\lambda)$ with respect to field samples collected in the nearshore ocean region (<20 m bottom depth) and overestimates $a_d(\lambda)$ in water with very low $a_d(\lambda)$ (Figures 6, 8, and 10). The gradients of high to low percentages of a_{ph} and a_d, and low to high percentage

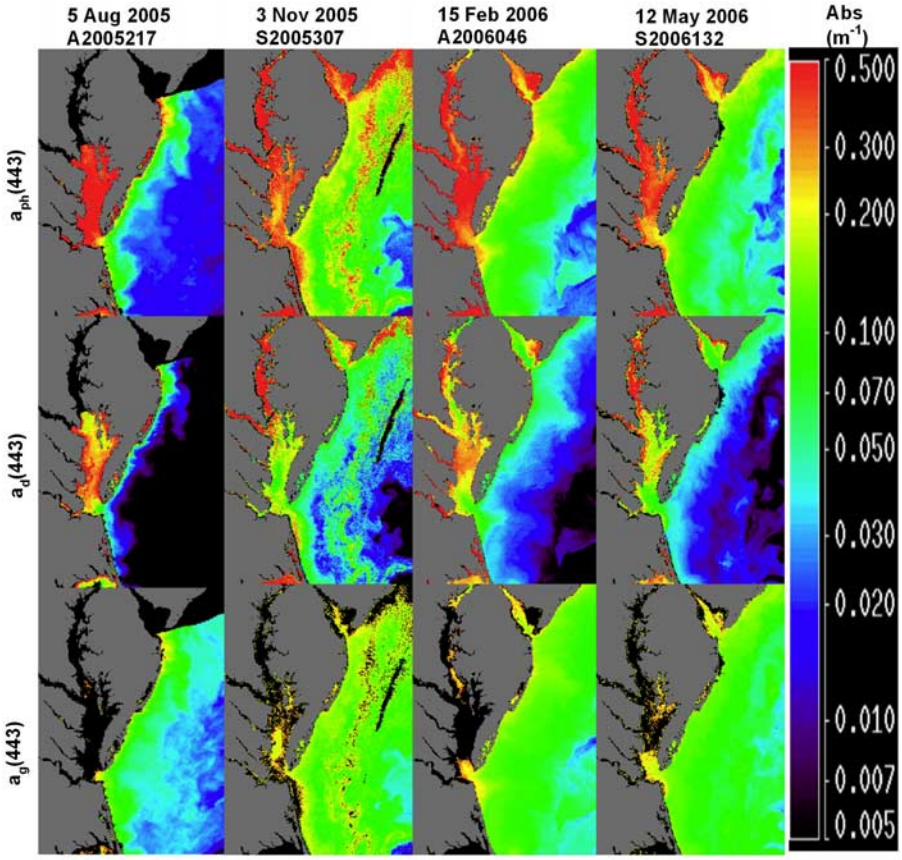

Figure 8. The distribution of a_{ph}, a_d, and a_g at 443 nm within the SMAB for 5 August and 3 November 2005, and 15 February and 12 May 2006 representing four seasons. The derived images for 5 August 2005 and 15 February 2006 were from MODIS-Aqua, while the other two were from SeaWiFS.

of a_g from the coast to the open ocean were consistent with field measurements (Figure 10). During the dry season (e.g., August 2005), CDOM accounts for a higher percentage of total absorption than during the wet season (e.g., February 2006) (Figure 9). Such a phenomenon may be explained by the impact of river discharge in contributing nutrients to support phytoplankton growth as well as the export of terrestrial CDOM. During the wet season, CDOM and phytoplankton abundance are both elevated, but phytoplankton blooms increase the relative percentage of phytoplankton absorption compared to CDOM absorption. During the dry season, CDOM and phytoplankton are both low, but the reported higher primary productivity and mature grazer community may result in a higher percentage of phytoplankton to be grazed and degraded which in turn reduces the relative percentage of phytoplankton absorption [*Adolf et al.*, 2006; *Marshall and Nesius*, 1996; *Marshall et al.*, 2006] and increase CDOM through grazer and microbial processing of organic matter [*Nelson et al.*, 2004; *Steinberg et al.*, 2004]. Since phytoplankton pigments have a much weaker relationship with CDOM absorption than with phytoplankton absorption, the significant contribution of CDOM absorption may pose complications for applying global operational algorithms (e.g., OC4V4 and OC3M) [*O'Reilly et al.*, 1998, 2000] to coastal regions. For CDOM-rich Case 2 waters such as the Chesapeake Bay, OC4V4 has been found to significantly overestimate [Chl_a], especially for offshore regions of the SMAB [*Harding et al.*, 2005; *Magnuson et al.*, 2004]. Our results also support this conclusion. For example, match-ups within ±8 hours showed that OC4V4 performed better for the lower CB region (e.g., CBH stations) with MAPD of 33.8% as compared to 79.6% for whole SMAB region (data not shown). It implies that the relative difference between our approach and operational algorithms would be relatively small in nearshore regions but high in offshore regions. The spatial distribution and the seasonal variability of [Chl_a] based on our approach displayed similar trends as those from OC4V4 and OC3M algorithms, but significantly reduced the overestimation by operational Chl_a algorithms in the offshore region of the SMAB (Figure 11). In general, the ratios of [Chl_a] based on operational Chl_a algorithms to our approach increase with the increase of CDOM contribution to light absorption (Figures 9 and 11). OC4V4 and OC3M [Chl_a] were higher by 0–0.5 times for the inner-shelf region, 0.4–1.2 times for the middle shelf region, and 1–2 times for the outer shelf region (Figure 11). This higher ratio trend toward offshore demonstrates the impact of CDOM on ocean color products in the SMAB.

[26] The satellite derivations of absorption coefficients provide tools to study biogeochemical processes and radiative transfer. For examples, DOC and salinity can be strongly correlated to CDOM absorption [*Del Vecchio and Blough*, 2004; *Mannino et al.*, 2008; *Rochelle-Newall and*

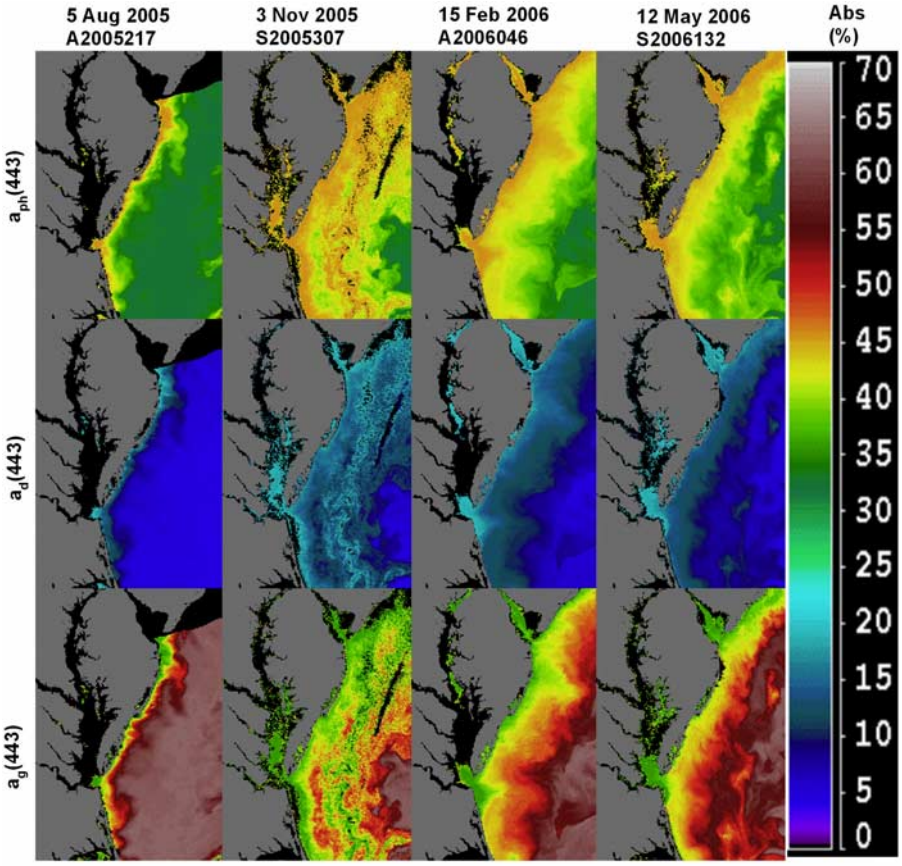

Figure 9. The distribution of the relative percentage of a_{ph}, a_d, and a_g to their sum at 443 nm within the SMAB. See Figure 8 for detail.

Fisher, 2002], and primary productivity is correlated to phytoplankton absorption [*Behrenfeld et al.*, 2005; *Marra et al.*, 2007]. The knowledge of absorption also provides methods to study other IOPs from space. For example, the expression of R_{rs} from absorption and backscattering [*Garver and Siegel*, 1997; *Gordon et al.*, 1988; *Maritorena et al.*, 2002] and the empirical expression of absorption from R_{rs} ratio make it possible to express backscattering into R_{rs}. The knowledge of backscattering might significantly improve the capability of semianalytical models in deriving ocean color products from space [*Magnuson et al.*, 2004].

[27] Although we have shown the significant impact of river discharge on biogeochemical constituents in the SMAB, the direct link between them should be interpreted with caution. First, the impact of river discharge on the coastal region of Chesapeake Bay is different from Delaware Bay. The lower Chesapeake Bay is subject to nutrient limitation for phytoplankton growth, in contrast to light availability in the Delaware Bay [*Harding et al.*, 1986; *Marshall and Alden*, 1993]. Therefore, an increase in river discharge is more likely to cause a phytoplankton bloom in the lower Chesapeake Bay by driving more nutrients downstream, while an increase in turbidity from higher river discharge may decrease primary production in the lower Delaware Bay. Second, the impact of river discharge is subject to seasonal variability and distance from the bay mouths, as shown in the following for the coastal region of

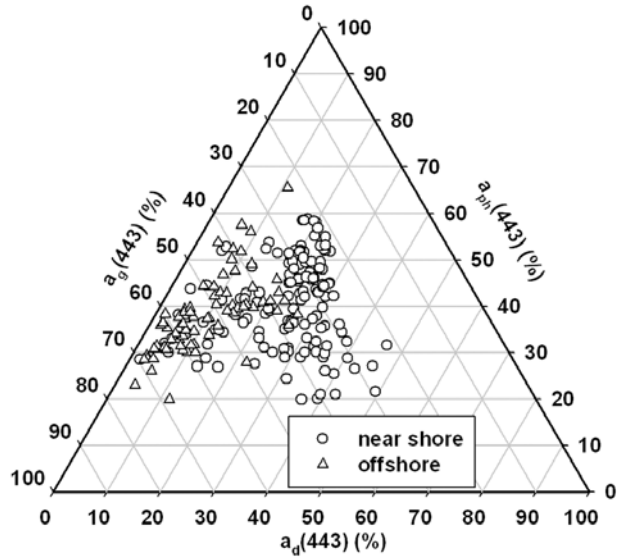

Figure 10. The relative percentage of a_{ph}, a_d, and a_g to their sum at 443 nm from field measurements grouped into two regions (nearshore region with bottom depth < 20 m and offshore region with bottom depth ≥ 20 m) within the SMAB.

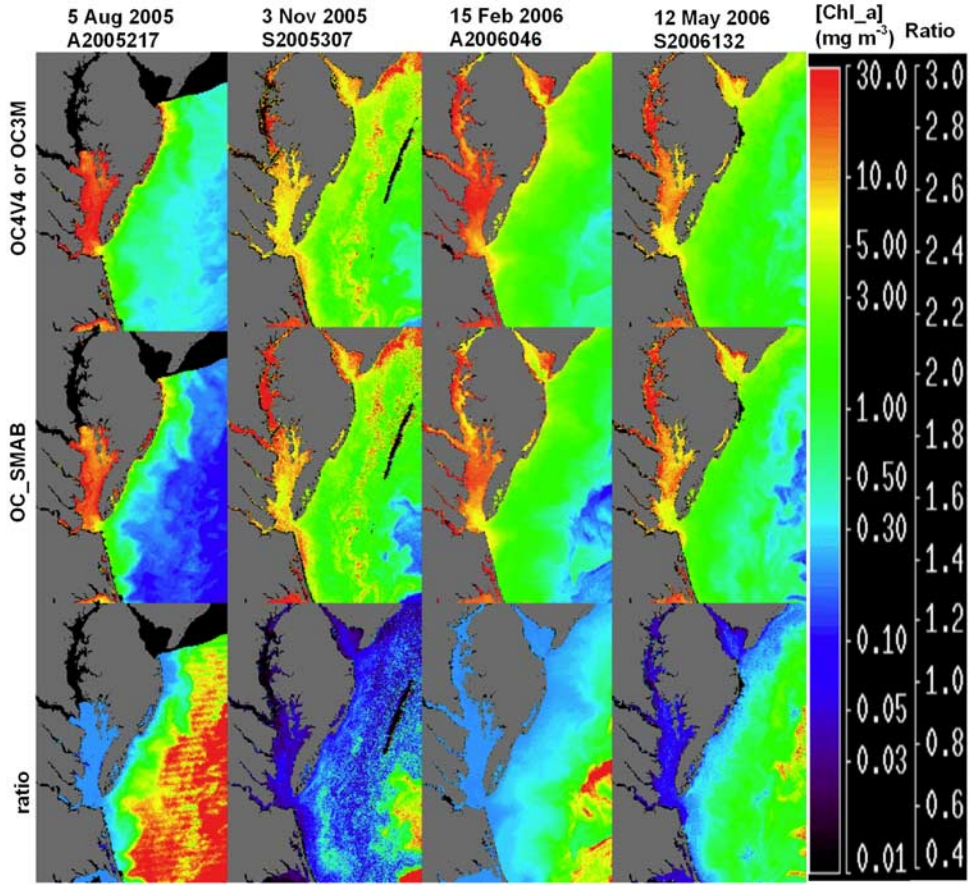

Figure 11. The distribution of [Chl_a] calculated from operational ocean color algorithms (OC4V4 for SeaWiFS and OC3M for MODIS-Aqua) and from the empirical method described in this paper (OC_SMAB; $[Chl\_a] = 70.632 \times [a_{ph}(670)]^{1.184}$) and their ratio [(OC4V4 or OC3M)/OC_SMAB] within the SMAB. See Figure 8 for detail. The responding scales of the color bar are in log units for [Chl_a] and in linear units for the ratio.

Chesapeake Bay. In the inner-shelf region, the correlation coefficients (r) between river discharge rate and biogeochemical products are low (e.g., r = 0.05–0.12 for [Chl_a] and −0.01–0.14 for a_g) for all seasons except for summer (Figure 12). The poor correlation may be due to averaging out the higher-frequency responses (less than one week) for the export of nutrients and CDOM, respectively, from the bays. During summer, the vertical stratification is well developed [*Verity et al.*, 2002], and the strength of river discharge represents the flux of nutrients for phytoplankton growth. Thus, the correlation between biogeochemical products and river discharge improves for summer (e.g., r = 0.48 for [Chl_a] and a_g) (Figure 12). In the middle shelf region, however, river discharge is significantly correlated to biogeochemical products in winter but poorly correlated during other seasons (e.g., r = 0.79 for [Chl_a] and a_g in winter and r = 0.09–0.36 in other seasons) (Figure 12). During winter, low water temperature and a less mature grazer community may cause the phytoplankton biomass to be linked directly to nutrient availability, which is driven primarily by river discharge and by wind-induced vertical mixing of nutrients from depth [*Adolf et al.*, 2006; *Marshall and Alden*, 1993]. As the zooplankton and bacterial communities develop into spring and summer, lower phytoplankton biomass and higher primary productivity are expected [*Adolf et al.*, 2006] and the direct response of the biological system to river discharge dissipates. The outer shelf region shows a similar pattern but a lower correlation coefficient (e.g., r = 0.49 for [Chl_a] and a_g in winter, and −0.13–0.31 in other seasons) with river discharge than the middle shelf region (data not shown).

[28] Other physical factors than river discharge, such as water temperature and wind forcing, anthropogenic activities, and even climate change, can also impact phytoplankton abundance, productivity, and carbon distributions in the SMAB. For example, the direction and distribution of the Chesapeake Bay plume is highly dependent on the wind stress direction. During winter and early spring northerly winds (downwelling favorable) and the alongshore southward current force the Chesapeake Bay [*Rennie et al.*, 1999; *Verity et al.*, 2002] and Delaware Bay [*Sanders and Garvine*, 2001] plumes to flow southward along the coast. As winds reverse later in spring the southerly alongshore flow weakens, and the Chesapeake Bay plume broadens and flows offshore, primarily to the south and east. Upwelling-favorable conditions can initiate local phytoplankton blooms and contribute additional particles to surface waters [*Johnson et al.*, 2001]. The Chesapeake Bay estuarine ecosystem has experienced a large increase in anthropogenic nutrient loading and reductions in the past half century

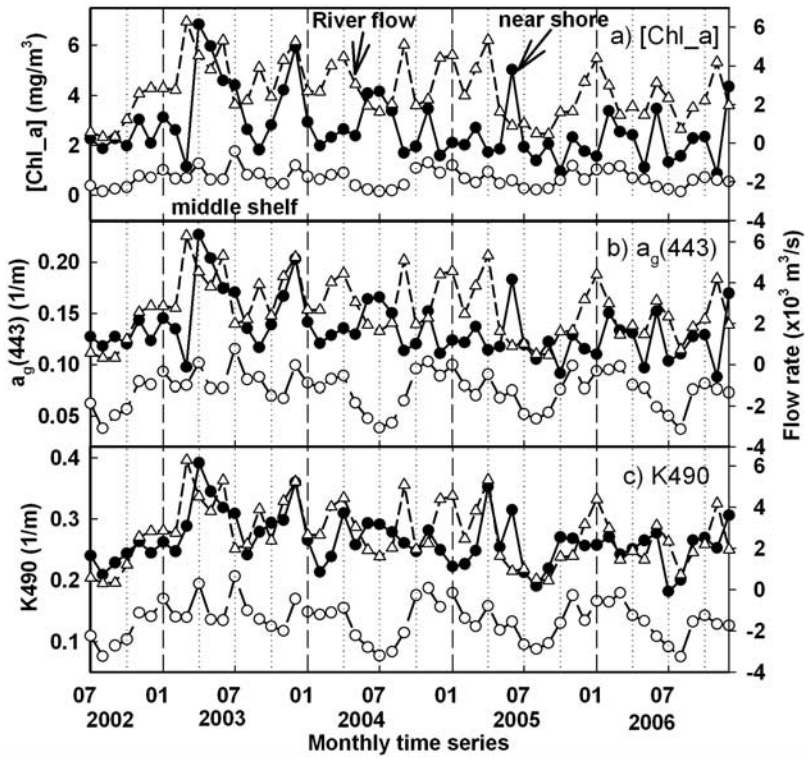

Figure 12. Monthly time series of (a) [Chl_a], (b) $a_g(443)$, and (c) diffuse attenuation coefficient at 490 nm (K490) from MODIS-Aqua Level-3 images (4 × 4 km resolution) for a nearshore location (75.90°W, 36.93°N) (solid circle) and a middle shelf location (75.30°W, 36.93°N) (open circle). [Chl_a] and $a_g(443)$ are calculated from algorithms developed in this paper, while K490 is a direct product from the Level-3 images. Monthly river discharge rates at the mouth of Chesapeake Bay (open triangle) (data is available at http://waterdata.usgs.gov/nwis/) (G. Fisher, U.S. Geological Survey, personal communication, 2007) are also shown for comparison.

which have affected the floral composition and biomass [*Harding*, 1994; *Paerl et al.*, 2006]. Furthermore, climate forcing (e.g., hurricanes, drought, etc.) significantly influences phytoplankton dynamics (e.g., by reducing vertical stratification, increasing sedimentary resuspension, and redistributing particles from hurricane forcing) [*Miller and Harding*, 2007; *Paerl et al.*, 2006].

[29] Above all, the impacts from physical factors (e.g., river discharge, wind forcing, and bathymetry) on bio-optical constituents (e.g., [Chl_a] and a_g) are complicated and cannot be explained by a single factor [*Harding*, 1994]. Nevertheless, we found that the variability of an optical property, the diffuse attenuation coefficient at 490 nm (K490), represents the variability of multiple bio-optical constituents. In the Chesapeake Bay inner-shelf site, the correlation coefficient (r) of [Chl_a], a_{ph}, a_d, a_g, and a_{dg} to K490 was 0.66–0.74, while 0.94–0.99 in the middle shelf location, and 0.93–0.98 in the outer shelf locations. These results also imply that absorption is the dominant contributor to the diffuse attenuation coefficient at offshore locations but scattering contributes significantly at nearshore locations.

4. Conclusions

[30] Several important conclusions can be made from the present analyses of absorption coefficients and [Chl_a] derived from ocean color remote sensing. The empirical algorithms demonstrate successful retrieval of absorption coefficients and [Chl_a] within a reasonable uncertainty (e.g., ±35%), and demonstrate significant improvements from the standard semianalytic model (e.g., GSM01 and GSM01-CB) and operational algorithms (e.g., OC4V4 and OC3M). Field observations and satellite derivations both demonstrate that CDOM is the major contributor to water column light absorption at shorter wavelengths (e.g., <500 nm), especially during the dry seasons and on the outer shelf where it can account for 35–70% of absorption by particles plus CDOM at 443 nm. River discharge plays a principal role in controlling the distribution of biogeochemical constituents, but is subject to seasonal and regional variability.

[31] **Acknowledgments.** This research was supported by an appointment to the NASA Postdoctoral Program at the Goddard Space Flight Center, administered by Oak Ridge Associated Universities through a contract with NASA. This work was funded with support from the NASA New Investigator Program, Interdisciplinary Science, and Earth Observing System programs and by NOAA through a grant in support of the Coastal Observatories program (NA03NOS4730220). We thank the captains and crews of R/V *Cape Henlopen*, R/V *Hugh R. Sharp*, and R/V *Fay Slover*. H. Throckmorton, P. Bernhardt, K. C. Filippino, C. Makinen, and M. Linksweiler provided assistance in collecting particulate samples. We are grateful to J. Morrow, J. Brown, D. D'Alimonte, and J.-N. Druon for deploying the profiling radiometer; to L. Van Heukelem and C. Thomas for

analyzing HPLC pigments; and the Ocean Biology Processing Group at GSFC. J. O'Reilly kindly provided the high-resolution bathymetry data.

References

Acker, J. G., L. W. Harding, G. Leptoukh, T. Zhu, and S. Shen (2005), Remotely sensed chl a at the Chesapeake Bay mouth is correlated with annual freshwater flow to the Chesapeake Bay, *Geophys. Res. Lett.*, *32*, L05601, doi:10.1029/2004GL021852.

Adolf, J. E., C. L. Yeager, W. D. Miller, M. E. Mallonee, and L. W. Harding (2006), Environmental forcing of phytoplankton floral composition, biomass, and primary productivity in Chesapeake Bay, USA, *Estuarine Coastal Shelf Sci.*, *67*, 108–122, doi:10.1016/j.ecss.2005.11.030.

Arrigo, K. R., and C. W. Brown (1996), Impact of chromophoric dissolved organic matter on UV inhibition of primary productivity in the sea, *Mar. Ecol. Prog. Ser.*, *140*, 207–216, doi:10.3354/meps140207.

Austin, J. (2002), Estimating the mean ocean-bay exchange rate of the Chesapeake Bay, *J. Geophys. Res.*, *107*(C11), 3192, doi:10.1029/2001JC001246.

Babin, M., A. Morel, V. Fournier-Sicre, F. Fell, and D. Stramski (2003a), Light scattering properties of marine particles in coastal and open ocean waters as related to the particle mass concentration, *Limnol. Oceanogr.*, *48*, 843–859.

Babin, M., D. Stramski, G. M. Ferrari, H. Claustre, A. Bricaud, G. Obolensky, and N. Hoepffner (2003b), Variations in the light absorption coefficients of phytoplankton, nonalgal particles, and dissolved organic matter in coastal waters around Europe, *J. Geophys. Res.*, *108*(C7), 3211, doi:10.1029/2001JC000882.

Bailey, S. W., and P. J. Werdell (2006), A multi-sensor approach for the on-orbit validation of ocean color satellite data products, *Remote Sens. Environ.*, *102*, 12–23, doi:10.1016/j.rse.2006.01.015.

Behrenfeld, M. J., E. Boss, D. A. Siegel, and D. M. Shea (2005), Carbon-based ocean productivity and phytoplankton physiology from space, *Global Biogeochem. Cycles*, *19*, GB1006, doi:10.1029/2004GB002299.

Bricaud, A., M. Babin, A. Morel, and H. Claustre (1995), Variability in the chlorophyll-specific absorption coefficients in natural phytoplankton: Analysis and parameterization, *J. Geophys. Res.*, *100*(C7), 13,321–13,332, doi:10.1029/95JC00463.

Bricaud, A., A. Morel, M. Babin, K. Allali, and H. Claustre (1998), Variations of light absorption by suspended particles with chlorophyll a concentration in oceanic (case 1) waters: Analysis and implications for bio-optical models, *J. Geophys. Res.*, *103*(C13), 31,033–31,044, doi:10.1029/98JC02712.

Carder, K. L., R. G. Steward, G. R. Harvey, and P. B. Ortner (1989), Marine humic and fulvic acids: Their effect on remote sensing of ocean chlorophyll, *Limnol. Oceanogr.*, *34*, 68–81.

Del Vecchio, R., and N. V. Blough (2004), Spatial and seasonal distribution of chromophoric dissolved organic matter (CDOM) and dissolved organic carbon (DOC) in the Middle Atlantic Bight, *Mar. Chem.*, *89*, 169–187, doi:10.1016/j.marchem.2004.02.027.

Duyens, L. N. M. (1956), The flattening of the absorption spectrum of suspensions as compared to that of solutions, *Biochim. Biophys. Acta*, *19*, 1–12, doi:10.1016/0006-3002(56)90380-8.

Ferrari, G. M., F. G. Bo, and M. Babin (2003), Geo-chemical and optical characterizations of suspended matter in European coastal waters, *Estuarine Coastal Shelf Sci.*, *57*, 17–24, doi:10.1016/S0272-7714(02)00314-1.

Garver, S. A., and D. A. Siegel (1997), Inherent optical property inversion of ocean color spectra and its biogeochemical interpretation: 1. Time series from the Sargasso Sea, *J. Geophys. Res.*, *102*(C8), 18,607–18,625, doi:10.1029/96JC03243.

Gordon, H. R., and A. Morel, (1983), *Remote Assessment of Ocean Color for Interpretation of Satellite Visible Imagery*, 114 pp., Springer, New York.

Gordon, H. R., O. B. Brown, R. H. Evans, J. W. Brown, R. C. Smith, K. S. Baker, and D. K. Clark (1988), A semianalytic radiance model o f ocean color, *J. Geophys. Res.*, *93*(D9), 10,909–10,924, doi:10.1029/JD093iD09p10909.

Harding, L., B. Messon, and T. Fisher (1986), Phytoplankton production in two east coast estuaries: Photosynthesis-light functions and patterns of carbon assimilation in Chesapeake and Delaware Bays, *Estuarine Coastal Shelf Sci.*, *23*, 773–806, doi:10.1016/0272-7714(86)90074-0.

Harding, L. W. (1994), Long-term trends in the distribution of phytoplankton in Chesapeake Bay: Roles of light, nutrients, and streamflow, *Mar. Ecol. Prog. Ser.*, *104*, 267–291, doi:10.3354/meps104267.

Harding, L. W., Jr., A. Magnuson, and M. E. Mallonee (2005), SeaWiFS retrievals of chlorophyll in Chesapeake Bay and the mid-Atlantic bight, *Estuarine Coastal Shelf Sci.*, *62*, 75–94, doi:10.1016/j.ecss.2004.08.011.

International Ocean-Colour Coordinating Group (IOCCG) (1999), Status and plans for satellite ocean-colour missions: Considerations for complementary missions, in *Reports of the International Ocean-Colour Coordinating Group*, edited by J. Yoder, *Rep. 2*, 43 pp., Dartmouth, N.S., Canada.

International Ocean-Colour Coordinating Group (IOCCG) (2000), Remote sensing of ocean color in coastal, and optically complex waters, in *Reports of the International Ocean-Colour Coordinating Group*, edited by S. Sathyendranath, *Rep. 3*, 140 pp., Dartmouth, N.S., Canada.

International Ocean-Colour Coordinating Group (IOCCG) (2006), Remote sensing of inherent optical properties: Fundamentals, tests of algorithms and applicaitons, in *Reports of the International Ocean-Color Coordinating Group*, edited by Z. Lee, *Rep. 5*, 126 pp., Dartmouth, N.S., Canada.

Jeffrey, S. W., R. F. C. Mantoura, and S. W. Wright, (1997). *Phytoplankton Pigments in Oceanography*, UNESCO, Paris.

Johnson, D. R., A. Weidemann, R. Arnone, and C. O. Davis (2001), Chesapeake Bay outflow plume and coastal upwelling events: Physical and optical properties, *J. Geophys. Res.*, *106*(C6), 11,613–11,622, doi:10.1029/1999JC000185.

Kirk, J. T. O., (1994), *Light and Phytosynthesis in Aquatic Ecosystems*, 2nd ed., Cambridge Univ. Press, New York.

Kishino, M., N. Takahashi, N. Okami, and S. Ichimura (1985), Estimation of the spectral absorption coefficient of phytoplankton in the sea, *Bull. Mar. Sci.*, *37*, 634–642.

Magnuson, A., L. W. Harding, M. E. Mallonee, and J. E. Adolf (2004), Bio-optical model for Chesapeake Bay and Middle Atlantic Bight, *Estuarine Coastal Shelf Sci.*, *61*, 403–424, doi:10.1016/j.ecss.2004.06.020.

Mannino, A., M. E. Russ, and S. B. Hooker (2008), Algorithm development and validation for satellite-derived distributions of DOC and CDOM in the U.S. Middle Atlantic Bight, *J. Geophys. Res.*, *113*, C07051, doi:10.1029/2007JC004493.

Maritorena, S., D. A. Siegel, and A. R. Peterson (2002), Optimization of a semianalytical ocean color model for global-scale applications, *Appl. Opt.*, *41*, 2705–2714, doi:10.1364/AO.41.002705.

Marra, J., C. C. Trees, and J. E. O'Reilly (2007), Phytoplankton pigment absorption: A strong predictor of primary productivity in the surface ocean, *Deep Sea Res., Part I*, *54*, 155–163, doi:10.1016/j.dsr.2006.12.001.

Marshall, H. G., and R. W. Alden (1993), A comparison of phytoplankton assemblages in the Chesapeake and Delaware estuaries (USA), with emphasis on diatoms, *Hydrobiologia*, *269-270*, 251–261, doi:10.1007/BF00028024.

Marshall, H. G., and K. K. Nesius (1996), Phytoplankton composition in relation to primary production in Chesapeake Bay, *Mar. Biol. Berlin*, *125*, 611–617.

Marshall, H. G., R. V. Lacouture, C. Buchanan, and J. M. Johnson (2006), Phytoplankton assemblages associated with water quality and salinity regions in Chesapeake Bay, USA, *Estuarine Coastal Shelf Sci.*, *69*, 10–18, doi:10.1016/j.ecss.2006.03.019.

McClain, C. R., G. C. Feldman, and S. B. Hooker (2004), An overview of the SeaWiFS project and strategies for producing a climate research quality global ocean bio-optical time series, *Deep Sea Res., Part II*, *51*, 5–42, doi:10.1016/j.dsr2.2003.11.001.

Miller, W. D., and L. W. Harding (2007), Climate forcing of the spring bloom in Chesapeake Bay, *Mar. Ecol. Prog. Ser.*, *331*, 11–22, doi:10.3354/meps331011.

Mitchell, B. G. (1990), Algorithms for determining the absorption coefficient of aquatic particulates using the quantitative filter technique (QFT), *Ocean Optics*, *X*, 137–148.

Mitchell, B. G., M. Kahru, J. Wieland, and M. Stramska, (2002), Determination of spectral absorption coefficients of particles, dissolved material and phytoplankton for discrete water samples, in *Ocean Optics Protocols for Satellite Ocean Color Sensor Validation, Revision 3*, vol. 2, edited by J. L. Mueller and G. S. Fargion, *Rep. NASA/TM-2002-210001/Rev3-Vol2*, pp. 231–257, NASA Goddard Space Flight Center, Greenbelt, Maryland.

Mobley, C., (1994), *Light and Water: Radiative Transfer in Natural Waters*, 592 pp., Elsevier, San Diego, Calif.

Mueller, J. L., (2000). SeaWiFS algorithm for the diffuse attenuation coefficient, K (490), using water-leaving radiances at 490 and 555 nm, in *SeaWiFS Postlaunch Calibration and Validation Analyses, Part 3*, vol. 11, edited by S. B. Hooker and E. R. Firestone, *Rep. NASA/TM-2000–206892*, pp. 24–27, NASA Goddard Space Flight Cent, Greenbelt, Md.

Nelson, N. B., C. A. Carlson, and D. K. Steinberg (2004), Production of chromophoric dissolved organic matter by Sargasso Sea microbes, *Mar. Chem.*, *89*, 273–289, doi:10.1016/j.marchem.2004.02.017.

O'Reilly, J. E., and C. Zetlin, (1998). Seasonal, horizontal, and vertical distribution of phytoplankton chlorophyll a in the northeast U.S. continental shelf ecosystem, *NOAA Tech. Rep. NMFS 139*, 120 pp., U.S. Dep. of Commer., Seattle, Wash.

O'Reilly, J. E., S. Maritorena, B. G. Mitchell, D. A. Siegel, K. L. Carder, S. A. Garver, M. Kahru, and C. McClain (1998), Ocean color algorithms for SeaWiFS, *J. Geophys. Res.*, *103*(C11), 24,937–24,953, doi:10.1029/98JC02160.

O'Reilly, J. E., et al. (2000), SeaWiFS postlaunch calibration and validation analyses, part 3, in *SeaWiFS Postlaunch Technical Report Series*, vol. 11, edited by S. B. Hooker and E. R. Firestone, *NASA Tech. Memo. 2000–206892*, NASA Goddard Space Flight Cent., Greenbelt, Md.

Paerl, H. W., L. M. Valdes, B. L. Peierls, J. E. Adolf, and L. W. Harding (2006), Anthropogenic and climatic influences on the eutrophication of large estuarine ecosystems, *Limnol. Oceanogr.*, *51*, 448–462.

Pope, R. M., and E. S. Fry (1997), Absorption spectrum (380–700 nm) of pure water. II. Integrating cavity measurements, *Appl. Opt.*, *36*, 8710–8723, doi:10.1364/AO.36.008710.

Prieur, L., and S. Sathyendranath (1981), An optical classification of coastal and oceanic waters based on the specific spectral absorption curves of phytoplankton pigments, dissolved organic-matter, and other particulate materials, *Limnol. Oceanogr.*, *26*, 671–689.

Rennie, S. E., J. L. Largier, and S. J. Lentz (1999), Observation of a pulsed buoyancy current downstream of Chesapeake Bay, *J. Geophys. Res.*, *104*(C8), 18,227–18,240, doi:10.1029/1999JC900153.

Rochelle-Newall, E. J., and T. R. Fisher (2002), Production of chromophoric dissolved organic matter fluorescence in marine and estuarine environments: An investigation into the role of phytoplankton, *Mar. Chem.*, *77*, 7–21, doi:10.1016/S0304-4203(01)00072-X.

Sanders, T. M., and R. W. Garvine (2001), Fresh water delivery to the continental shelf and subsequent mixing: An observational study, *J. Geophys. Res.*, *106*(C11), 27,087–27,101, doi:10.1029/2001JC000802.

Siegel, D. A., M. Wang, S. Maritorena, and W. D. Robinson (2000), Atmospheric correction of satellite ocean-color imagery: The black pixel assumption, *Appl. Opt.*, *39*, 3582–3591, doi:10.1364/AO.39.003582.

Siegel, D. A., S. Maritorena, N. B. Nelson, D. A. Hansell, and M. Lorenzi-Kayser (2002), Global distribution and dynamics of colored dissolved and detrital organic materials, *J. Geophys. Res.*, *107*(C12), 3228, doi:10.1029/2001JC000965.

Siegel, D. A., S. Maritorena, N. B. Nelson, and M. J. Behrenfeld (2005), Independence and interdependencies among global ocean color properties: Reassessing the bio-optical assumption, *J. Geophys. Res.*, *110*, C07011, doi:10.1029/2004JC002527.

Signorini, S. R., C. R. McClain, A. Mannino, and S. Bailey, (2005), Report on ocean color and carbon study for the south Atlantic Bight and Chesapeake Bay regions, *Rep. NASA/TM-2005–212787*, NASA Goddard Space Flight Cent., Greenbelt, Md.

Steinberg, D. K., N. B. Nelson, C. A. Carlson, and A. C. Prusak (2004), Production of chromophoric dissolved organic matter (CDOM) in the open ocean by zooplankton and the colonial cyanobacterium *Trichodesmium* spp., *Mar. Ecol. Prog. Ser.*, *267*, 45–56, doi:10.3354/meps267045.

Trees, C. C., D. K. Clark, R. R. Bidigare, M. E. Ondrusek, and J. L. Mueller (2000), Accessory pigments versus chlorophyll a concentration with the euphotic zone: A ubiquitous relationship, *Limnol. Oceanogr.*, *45*, 1130–1143.

Van Heukelem, L., and C. S. Thomas (2001), Computer-assisted high-performance liquid chromatography method development with applications to the isolation and analysis of phytoplankton pigments, *J. Chromatogr. A*, *910*, 31–49, doi:10.1016/S0378-4347(00)00603-4.

Verity, P. G., J. E. Bauer, C. N. Flagg, D. J. DeMaster, and D. J. Repeta (2002), The Ocean Margins Program: An interdisciplinary study of carbon sources, transformations, and sinks in a temperate continental margin system, *Deep Sea Res., Part II*, *49*, 4273–4295, doi:10.1016/S0967-0645(02)00120-0.

S. B. Hooker, A. Mannino, X. Pan, and M. E. Russ, NASA Goddard Space Flight Center, Mail Code 614.7, Building 22, Room 248, Greenbelt, MD 20771, USA. (xpan@neptune-web.gsfc.nasa.gov)